JOURNAL OF AIRCRAFT
Vol. 35, No. 5, September–October 1998

Wing-Tip Vortex Calculations Using a High-Accuracy Scheme

David P. Lockard* and Philip J. Morris†
Pennsylvania State University, University Park, Pennsylvania 16802

The objective of the research described in this paper is to investigate the use of computational aeroacoustics methodology and parallel computers to simulate the development of a tip vortex. A three-dimensional Euler code, implemented using the message passing library and Fortran 90 on the IBM SP2, is used to perform calculations of the steady flow. Results are presented for low-speed flow over a finite span NACA 0012 wing. Comparisons with experimental data show that the tip vortex is predicted to diffuse too rapidly, but the high-accuracy scheme does reduce numerical errors. It is argued that Navier–Stokes calculations on a much finer mesh would improve the solutions, but they would be prohibitively expensive for unsteady calculations.

Nomenclature

AR	=	aspect ratio
b	=	wing span
C_L	=	wing lift coefficient
c_p	=	pressure coefficient, $(p - p_\infty)/(1/2\rho_\infty \lvert \boldsymbol{V}_\infty \rvert^2)$
$\mathcal{D}$	=	discrete form of the artificial dissipation
$\mathcal{F}$	=	discrete form of the spatial derivatives
F_L	=	wing lift force
h	=	mesh spacing
J	=	Jacobian
l	=	chord length
LE	=	leading edge
M	=	Mach number
$\boldsymbol{n}$	=	normal vector
p	=	pressure
$\boldsymbol{Q}$	=	vector of dependent variables
S	=	wing planform area
t	=	time
u, v, w	=	Cartesian velocity components
x, y, z	=	Cartesian coordinates
α	=	angle of attack
Γ	=	circulation
γ	=	ratio specific heats
κ, $\nu_{\max}$, k_0, β_0	=	scaling coefficients for the artificial dissipation
ν, ϕ, χ	=	switches for the artificial dissipation
ξ, η, ζ	=	generalized coordinates
ρ	=	density

Introduction

IN this paper calculations of the steady flow over a finite wing are performed using the high-order spatial operators of a computational aeroacoustics (CAA) scheme and an explicit, time-marching algorithm. These solutions provide the basis for future analyses of noise-generation mechanisms involving a wing-tip vortex or flap side-edge.

To perform acoustic calculations all of the transients in the mean flow need to be removed from the domain. If aerodynamic fluctuations persist, one is unable to identify the acoustics in the problem without taking extensive samples of the data. This is one of the additional complications encountered when using a fully numerical technique to solve for the total variables in the simulation of acoustic phenomena. In the current approach a time-independent solution is obtained for the mean field. This is then used as the starting solution in subsequent simulations of the unsteady problem. This approach has been applied successfully by the authors to calculate the noise radiated by unsteady vortical gusts encountering airfoils.[1] CAA algorithms are designed to minimize dissipation and dispersion, so they are inefficient at converging to a steady state. However, because the time integration does not affect the steady solution, local time stepping with modified Runge–Kutta (RK) coefficients may be used to improve the damping characteristics and accelerate the movement of information within the domain. To further enhance the convergence, a multigrid method is employed. Once the converged steady state is obtained, it may be used as the initial flowfield in a time-accurate calculation. The results presented in this paper illustrate the capability of high-accuracy spatial operators to capture a flowfield that includes a tip vortex, and exemplify the difficulties of performing future time-accurate analyses of problems involving a wing.

Although the ultimate goal of the current research is to simulate problems involving acoustics, the accurate calculation of the steady flow is equally important and can have a significant impact on acoustic phenomena. Furthermore, much can be learned from the physics involved in wing-tip vortex problems. Even in steady flow, the tip vortex has a strong influence on the mean aerodynamics. Unsteadiness within the vortex also plays an important role in the generation of sound. George et al.[2] proposed that the turbulence in the tip vortex and the separated region around the tip passes over the trailing edge and causes noise. Any incoming disturbance is also likely to be modified by the presence of the vortex. Unfortunately, previous numerical simulations have had difficulty in generating tip vortices of the correct strength and in preserving them as they convect off the wing. Accurate simulations of this wake are necessary for blade vortex interactions and fuselage interactions to be studied. Part of the difficulty has been the predominant use of low-order schemes with high values of numerical dissipation on highly stretched grids. Kramer et al.[3] and Srinivasan et al.[4] performed calculations for hovering rotors using the Euler and thin-layer Navier–Stokes equations, respectively. They found that the surface pressures were in good agreement with experiment, but the wakes diffused much too rapidly. Thus, if one is only interested in cases where no vortex interactions occur, the Euler equations are sufficient to obtain realistic surface pressures. However, as Strawn[5] noted

Received Sept. 10, 1997; revision received April 1, 1998; accepted for publication April 15, 1998.

*Graduate Research Assistant, Department of Aerospace Engineering; currently Research Scientist, NASA Langley Research Center, Hampton, VA 23681. E-mail: d.p.lockard@larc.nasa.gov. Member AIAA.

†Boeing/A.D. Professor, Department of Aerospace Engineering. E-mail: pjm@psu.edu. Associate Fellow AIAA.

from his Euler calculations on unstructured grids, Euler simulations always produce vortex cores that are too large and peak velocities that are too small. This is because viscous effects at the tip play an important role in the formation of the vortex. At the tip, fluid particles from below the wing are pushed around the tip into the low-pressure region on the upper surface. These particles undergo considerable acceleration and deceleration during this migration. These gradients produce significant viscous effects that alter the particle trajectories. However, to perform calculations with enough grid resolution near the tip has been intractable for these large, three-dimensional problems because of computational resource limitations.

Some of the experimental studies in this area includes work by Francis and Kennedy,[6] Felker et al.,[7] McAlister and Takahashi,[8] and Shekarriz et al.[9] These studies show that the tip vortex rolls up tightly and moves away from the tip while convecting over the upper surface. Devenport et al.[10] made measurements of tip vortex structures and concluded that the vortex core is laminar. Even though the outer region is turbulent, a turbulence model should not be needed to capture the general characteristics of the vortex formation and initial propagation within a few chord lengths from the wing. However, turbulence modeling will be necessary farther downstream and to simulate interactions of turbulence with the wing.

Because it has been shown that the surface pressure may be computed fairly accurately using the Euler equations, the calculations presented here are inviscid. It is believed that the present inviscid calculations demonstrate an ability to preserve the vortex wake better than typical computational fluid dynamics (CFD) methods. However, even the inviscid problem is formidable. Not only are the computational demands high, typical wing grids from CFD are not sufficiently smooth for CAA applications. Most CFD grids have singularity points in the vicinity of the tip. The current method is unstable around these singularities. Therefore, an H–H mesh is used. Although these meshes do not possess any singularities, they are discontinuous in the first derivative at the leading edge. Therefore, special treatment is required in this region for the code to produce acceptable solutions. Furthermore, the H–H meshes for the wing need to be generated in two blocks: One for the upper surface and one for the lower.

In this paper the equations of motion in three dimensions are given. Then the solution algorithm is discussed and some discussion of the procedures for dealing with the discontinuity in the grid metrics on H meshes is included. Some of the details for dealing with multiple blocks are also addressed. The majority of the paper is devoted to three-dimensional results for low-speed flow over a NACA 0012 wing. Comparisons are made with experiment whenever possible. The growth of the vortex is found to be much larger than that measured in experiment, but many of the other parameters are well predicted.

Numerical Algorithm

The Fortran 90 code used in this research is written for parallel computers using the message passing interface (MPI). A detailed description of the parallel implementation can be found in a previous paper by the authors.[11] The explicit time-stepping algorithm employed in this work can be programmed efficiently to run on a collection of workstations such as the IBM SP2. More information about the algorithm can be found in Lockard.[12]

Governing Equations

The Euler equations may be used to describe acoustic phenomena and are used for the current steady calculations. In addition, to simulate flows around curved bodies, such as wings, generalized coordinates are used. The dimensionless equations of motion in three dimensions may be written as

$$\begin{aligned}
&\frac{\partial \rho}{\partial t} + u\frac{\partial \rho}{\partial x} + v\frac{\partial \rho}{\partial y} + w\frac{\partial \rho}{\partial z} + \rho\left(\frac{\partial u}{\partial x} + \frac{\partial v}{\partial y} + \frac{\partial w}{\partial z}\right) = 0\\
&\frac{\partial p}{\partial x} + u\frac{\partial p}{\partial x} + v\frac{\partial p}{\partial y} + w\frac{\partial p}{\partial z} + \gamma p\left(\frac{\partial u}{\partial x} + \frac{\partial v}{\partial y} + \frac{\partial w}{\partial z}\right) = 0\\
&\frac{\partial u}{\partial t} + u\frac{\partial u}{\partial x} + v\frac{\partial u}{\partial y} + w\frac{\partial u}{\partial z} + \frac{1}{\rho}\frac{\partial p}{\partial x} = 0\\
&\frac{\partial v}{\partial t} + u\frac{\partial v}{\partial x} + v\frac{\partial v}{\partial y} + w\frac{\partial v}{\partial z} + \frac{1}{\rho}\frac{\partial p}{\partial y} = 0\\
&\frac{\partial w}{\partial t} + u\frac{\partial w}{\partial x} + v\frac{\partial w}{\partial y} + w\frac{\partial w}{\partial z} + \frac{1}{\rho}\frac{\partial p}{\partial z} = 0
\end{aligned} \tag{1}$$

The fluid is assumed to be an ideal gas. The Euler equations and the ideal gas law form a complete set of equations that may be solved for the dependent variables. γ is taken as 1.4. These dimensionless equations use the speed of sound as the reference velocity and the airfoil chord as the length scale.

A transformation from (x, y, z) to (ξ, η, ζ) space is applied to the equations by expanding the spatial derivatives using the chain rule. For example, the derivative in the x direction is given by $\partial/\partial x = \xi_x(\partial/\partial\xi) + \eta_x(\partial/\partial\eta) + \zeta_x(\partial/\partial\zeta)$. The subscripts on the generalized coordinates denote partial differentiation. The resulting equations can be solved efficiently by grouping like terms. J denotes the Jacobian of the transformation.

Solution Algorithm

The governing equations can be written in the semidiscrete, compact form

$$\frac{\partial \boldsymbol{Q}}{\partial t} = -[\mathcal{F}(\boldsymbol{Q}) - \mathcal{D}(\boldsymbol{Q})] = -\mathcal{R}(\boldsymbol{Q}) \tag{2}$$

Here, $\mathcal{F}$ represents the discrete form of all the spatial derivatives appearing in the governing equations. The spatial operator can either be sixth-order or possess the dispersion-relation-preserving (DRP) property developed by Tam and Webb.[13] All of the calculations presented in this purpose use the DRP coefficients of Lockard et al.[14] Linearized RK time integration of the following form is used to advance the solution in time:

$$\begin{aligned}
\boldsymbol{Q}^{(1)} &= \boldsymbol{Q}^n\\
\boldsymbol{Q}^{(s)} &= \boldsymbol{Q}^n - \alpha_s \Delta t\{\mathcal{F}[\boldsymbol{Q}^{(s-1)}] - \mathcal{D}[\boldsymbol{Q}^{(0)}]\}\\
\boldsymbol{Q}^{n+1} &= \boldsymbol{Q}^{s_{\max}}
\end{aligned} \tag{3}$$

The superscript n denotes the time step, and s is a stage counter that runs from 1 to $s_{\max}$. For steady-state calculations, $s_{\max} = 4$ with $\alpha = [0.375, 0.5, 1.0, 1.0]$. These coefficients give good damping characteristics over a wide range of wave numbers. Other common choices for the α do not yield any significant improvement in the stability limit for the present scheme because of the large extent of the spatial operators. The local time step is chosen based on the Courant–Freidrichs–Lewy (CFL) constraint

$$\Delta t = \frac{\mathrm{CFL}}{(|U| + c|\nabla\xi|) + (|V| + c|\nabla\eta|) + (|W| + c|\nabla\zeta|)} \tag{4}$$

The CFL number is typically chosen to be 1.1.

Riemann invariant[15] boundary conditions are used at subsonic inflow boundaries for steady calculations. The method of characteristic conditions developed by Thompson[16] are ap-

plied at outflow boundaries. Furthermore, characteristic conditions are applied for inviscid walls.

Artificial Dissipation

Because central-difference operators do not possess any implicit dissipation, a filter has been added explicitly. A higher-order version of the adaptive dissipation of Jameson et al.[17] has been implemented for this purpose. An optimized smoother using a seven-point stencil is used as a background dissipation rather than the fourth derivative used in Jameson's implementation. This smoother, denoted by $\partial^0/\partial\xi^0$, is given by Tam and Dong[18] for a Gaussian half-width of $\sigma = 0.3\pi$. It has been scaled by 155 in the current implementation to make its level more similar to the traditional fourth- and sixth-derivative operators. This scaled operator is given by

$$\frac{\partial^0 f}{\partial \xi^0} = D_3^0(f_{i+3} + f_{i-3}) + D_2^0(f_{i+2} + f_{i-2}) + D_1^0(f_{i+1} + f_{i-1}) + D_0^0 f_i \tag{5}$$

where

$$\begin{aligned} D_3^0 &= 2.8782787434202, & D_2^0 &= -15.483962878993 \\ D_1^0 &= 36.432863910249, & D_0^0 &= -47.6543595493524 \end{aligned} \tag{6}$$

i is used as the index of the discrete points in the ξ direction. Recall that the step size is unity in the computational plane. Standard second- and fourth-derivative dissipation is also employed near discontinuities and boundaries.

Many switches for the artificial dissipation have been investigated that are more appropriate for acoustical calculations. Switches designed purely for acoustics are found to perform poorly for steady-state calculations because they are too sensitive to the wave-number properties of the flow. A new switch has been implemented here that accounts for the needs of the two calculations. It has been used successfully to converge flows with shocks and still maintain better properties for acoustics. The dissipation is defined in the nonconservative form as

$$\mathcal{D} = \mathcal{D}_\xi + \mathcal{D}_\eta + \mathcal{D}_\zeta \tag{7}$$

where the terms in the ξ direction are

$$\begin{aligned} \mathcal{D}_\xi &= (|U| + c\sqrt{\xi_x^2 + \xi_y^2 + \xi_z^2})\left(\varepsilon_2 \frac{\partial^2}{\partial \xi^2} + \varepsilon_0 \frac{\partial^0}{\partial \xi^0}\right) \\ \nu_i &= \min\left(d_2, \frac{\kappa}{p_i}\frac{\partial^4 p_i}{\partial \xi^4}\right), \qquad \nu_{\max} = \max(\nu_{i-1}, \nu_i, \nu_{i+1}) \\ \varepsilon_2 &= \max[0, 4(\nu_{\max} - \nu_2)], \qquad \varepsilon_0 = \max(0, d_0 + \phi - 2\varepsilon_2) \end{aligned} \tag{8}$$

Analogous expressions are used in the η and ζ directions. The term ϕ is used to increase the coefficient of the basic smoother linearly in a regime when the second derivative dissipation is off, but low-amplitude waves are poorly represented on the grid. It is given by

$$\phi = \chi \beta_0 d_0^{\max} \tag{9}$$

where

$$\begin{aligned} \chi &= \min[\beta_1, \max(0, \nu_{\max} - \nu_0)] \\ \beta_0 &= (0.1\nu_2 - \nu_0), \qquad \beta_1 = \max(0, 1/\beta_0) \end{aligned} \tag{10}$$

The scaling factors β_0 and β_1 are calculated once and stored, and so they do not add much work to the calculations. In the current implementation, $\kappa = 0.3$ is a scaling coefficient for the switch. $d_0 = 1e-3$ is the background level of the basic smoother. The background smoother begins increasing above its background level when the switch exceeds $\nu_0 = 1e-5$. $d_0^{\max} = 0.01$ is the maximum allowable value of the background smoother. d_2 fixes the maximum allowable value of the second-derivative dissipation and is set to 0.15. $\nu_2 = 0.02$ defines a threshold value below which no second-order dissipation is used.

At boundaries the dissipation stencil is decreased from seven to five and then to three points. Hence, the sixth-derivative, fourth-derivative, and then the second-derivative dissipation are utilized in the normal direction to a boundary as the boundary is approached. No dissipation is applied normal to a boundary on grid lines that represent inflow and outflow boundaries. A constant scaling factor of $7e-3$ is used for the three points at the boundary using the different dissipation operators. However, at solid walls dissipation is applied at the wall. Because large gradients tend to exist there, having no dissipation at the wall produces poor results. Using extrapolated values for a ghost cell inside the wall allows a second-derivative dissipation to be applied at the wall, but it reduces to the identical dissipation applied at the neighboring point when quadratic extrapolation is used. Applying the negative of the neighbor's second-derivative dissipation is used instead because this tends to reduce the variations between the wall and its neighbor. The scaling coefficient at the wall at the adjacent point is 0.03. The fourth- and sixth-derivatives use 0.02 and 0.01, respectively.

Multigrid Acceleration

Jameson's full approximation storage (FAS) method[19] is used to accelerate convergence to a steady-state of the Euler equations. Because CAA algorithms are designed to preserve wave-like phenomena, they are poorly suited to obtain steady solutions. Thus, multigrid and other acceleration techniques that preserve the spatial accuracy need to be exploited.

Basic to any multigrid scheme are transfer operators. The full weighting operator is used to restrict the residual.[20] In addition, the Jacobian is used as a weighting factor. In one dimension, the restriction of the residual is given by

$$\frac{\mathcal{R}_{2h}^{\,i}}{J_{2h}^{i}} = 2\,\frac{1}{4}\left(\frac{\mathcal{R}_h^{2i-1}}{J_h^{2i-1}} + 2\,\frac{\mathcal{R}_h^{2i}}{J_h^{2i}} + \frac{\mathcal{R}_h^{2i+1}}{J_h^{2i+1}}\right) \tag{11}$$

The superscript denotes the grid point, and i ranges from 0 to $N/2 - 1$. N represents the grid size on the fine mesh. In three dimensions the restriction operator is applied once in each direction. Direct injection is used for the solution variables. Furthermore, all grid parameters, such as the metrics, are restricted by simply scaling directly injected values.

The correction to the solution is prolonged from a coarse mesh to a fine mesh using bilinear interpolation. This correction is the difference between the current solution on the coarse mesh and the starting one obtained by restricting the fine-grid solution.

By using these operators to transfer information between meshes, a multilevel algorithm may be implemented. The stages of the RK scheme on a coarse mesh, $2h$, are given by

$$\boldsymbol{Q}_{2h}^{(s)} = \boldsymbol{Q}_{2h}^{(0)} - \alpha_s \Delta t_{2h}\{\mathcal{F}[\boldsymbol{Q}_{2h}^{(s-1)}] - \mathcal{D}[\boldsymbol{Q}_{2h}^{(0)}] + \mathcal{P}_{2h}\} \tag{12}$$

where $\mathcal{P}_{2h}$ is a forcing function defined by

$$\mathcal{P}_{2h} = \mathcal{W}_h^{2h}[\mathcal{F}_h(\boldsymbol{Q}_h) - \mathcal{D}_h(\boldsymbol{Q}_h) + \mathcal{P}_h] - \{\mathcal{F}_{2h}[\boldsymbol{Q}_{2h}^{(0)}] - \mathcal{D}_{2h}[\boldsymbol{Q}_{2h}^{(0)}]\} \tag{13}$$

The forcing function on the fine mesh, $\mathcal{P}_h$, is zero. Because the forcing function contains the residual of the coarse mesh from the first RK stage, the solution on the coarse mesh will be driven by the fine-grid residual. This can be exploited by using a different scheme on coarser meshes. A second-order, central-difference spatial operator with a constant-coefficient,

second-derivative dissipation is used on all coarse meshes. This allows the CFL number to be increased to 1.8 on coarser meshes and further reduces the work. The communication is also reduced because the number of planes of data needed to accommodate the standard stencil at a processor interface is reduced from three to unity.

The process may be repeated for as many meshes as desired, but only a maximum of four levels have been used successfully with the current code. The finest mesh is chosen to have $2n + 1$ points in each direction, where n is an integer. This allows the boundaries to be maintained as the grid is reduced. A three-level, sawtooth cycle is used with two RK iterations on the coarsest mesh, and one on all other meshes. All boundary conditions are applied after every restriction and prolongation of the solution variables. The solution is started on the finest mesh with the sawtooth cycles continuing until convergence is obtained.

Steady Three-Dimensional Solutions for a NACA 0012 Wing

Steady, inviscid solutions for a NACA 0012 wing are investigated to substantiate the possibility of performing unsteady calculations in three dimensions using a CAA method. The span of the rectangular wing is 8.54 when normalized by the chord length. Because the chord is used as the reference length, AR is also 8.54. The tip is rounded to minimize the discontinuity in the grid in that region. The H–H mesh for the calculations has been obtained using version 11 of the program Gridgen. The x and y directions coincide with the airfoil chord and its normal, respectively. z is used in the spanwise direction. Only half of the wing is included in the simulation. A symmetry condition is applied at the root plane that passes through the center of the wing. This plane can be seen in Fig. 1, where the x–y planes of the edge of the computational domain are

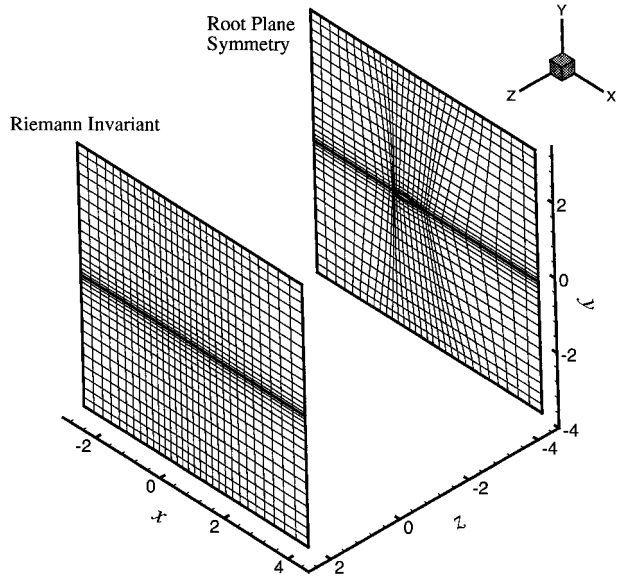

Fig. 1 x–y planes of a grid for a NACA 0012 wing.

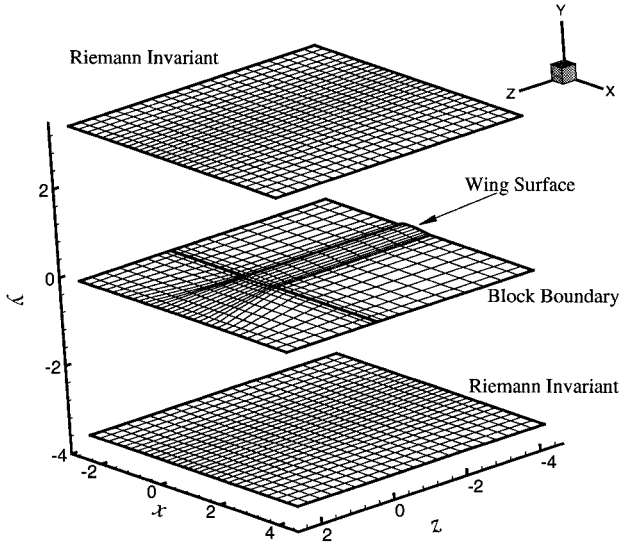

Fig. 2 x–z planes of a grid for a NACA 0012 wing.

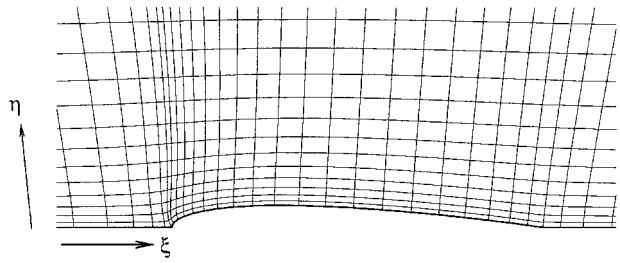

Fig. 3 H grid for a NACA 0012 airfoil.

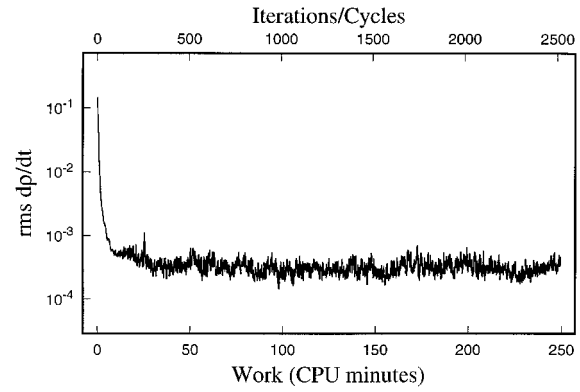

Fig. 4 Convergence history for three levels of multigrid on 16 processors. NACA 0012 wing with $M = 0.117$, $\alpha = 5$ deg, $b = 8.54$.

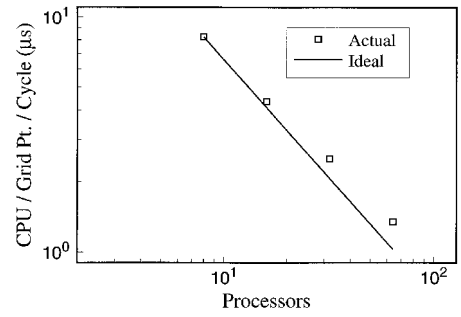

Fig. 5 Scalability study for the three-dimensional multigrid code.

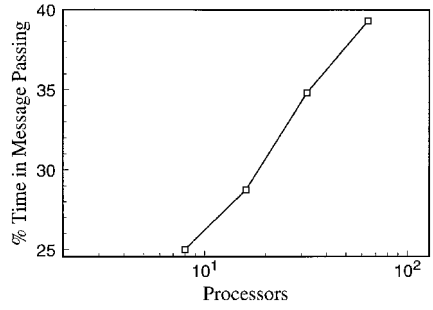

Fig. 6 Time spent passing messages for three-dimensional multigrid code using three levels.

shown. The grid has been reduced by a factor of 4 in each direction and has been truncated for plotting purposes. The actual domain extends to $x = 10$ in the streamwise direction. The leading edge of the tip corresponds to the (x, y, z) point of (0, 0, 0). Because the tip is actually a circular arc, the actual maximum extent of the wing tip is at a z location of 0.12, which corresponds to the thickness of the NACA 0012 airfoil. Along the maximum z plane, Riemann invariant boundary conditions are used.[15] The x–z planes for the computations are shown in Fig. 2. Riemann invariant conditions are applied on the the upper and lower boundaries. At the center of the domain is the wing and the interface between the upper and lower halves of the blocks of the H–H meshes. Along the wing surface, slip-wall conditions are applied. Everywhere else along that plane data are transferred between the two blocks. The solution along the interface is obtained by averaging the solutions from the two blocks.

The primary difficulty with H grids is the discontinuity in the metrics at the leading edge of the airfoil. Figure 3 shows a close-up view of the mesh around the airfoil. At the leading edge, the grid line turns by 90 deg. Hence, this is a singular point in the mapping. Because the high-accuracy operators used in this paper assume that all quantities are smooth, any derivatives across this point would be incorrect. Therefore, the stencils in the vicinity of the leading edge must be modified so that they do not cross the singular point. The bottom boundary corresponds to a η_{min} edge. At the singular point it is a ξ line that is normal to the airfoil surface. Therefore, that point is solved as if it were a ξ_{max} boundary with a fully biased operator. The stencils for the ξ derivatives at the left and right adjacent points use biased operators that do not cross the singular point. The order of the discretization is reduced to second-order at the singular point. The order of the dissipation is also reduced so that the dissipation stencil encompasses the same range as the stencil used for the derivatives of the flow variables. Derivatives in the η direction along the block boundary require information from the other block. Hence, this is considered a message-passing type of boundary. The main difference is that the solution is averaged along the block interface after each RK stage. Also, the η derivative at the singular point is second order. The finite difference, derivative operators used to generate the metrics are also modified in an identical manner. A similar procedure is applied at the wing tip.

The operating conditions for the simulation are chosen to match those used by Devenport et al.[10] in their experiments. The Mach number of the flow is 0.117, and the angle of attack is $\alpha = 5$ deg. In the numerical simulations the freestream vector is rotated by 5 deg to simulate the angle of attack. Thus, there is a mean component of velocity in both the x and y directions.

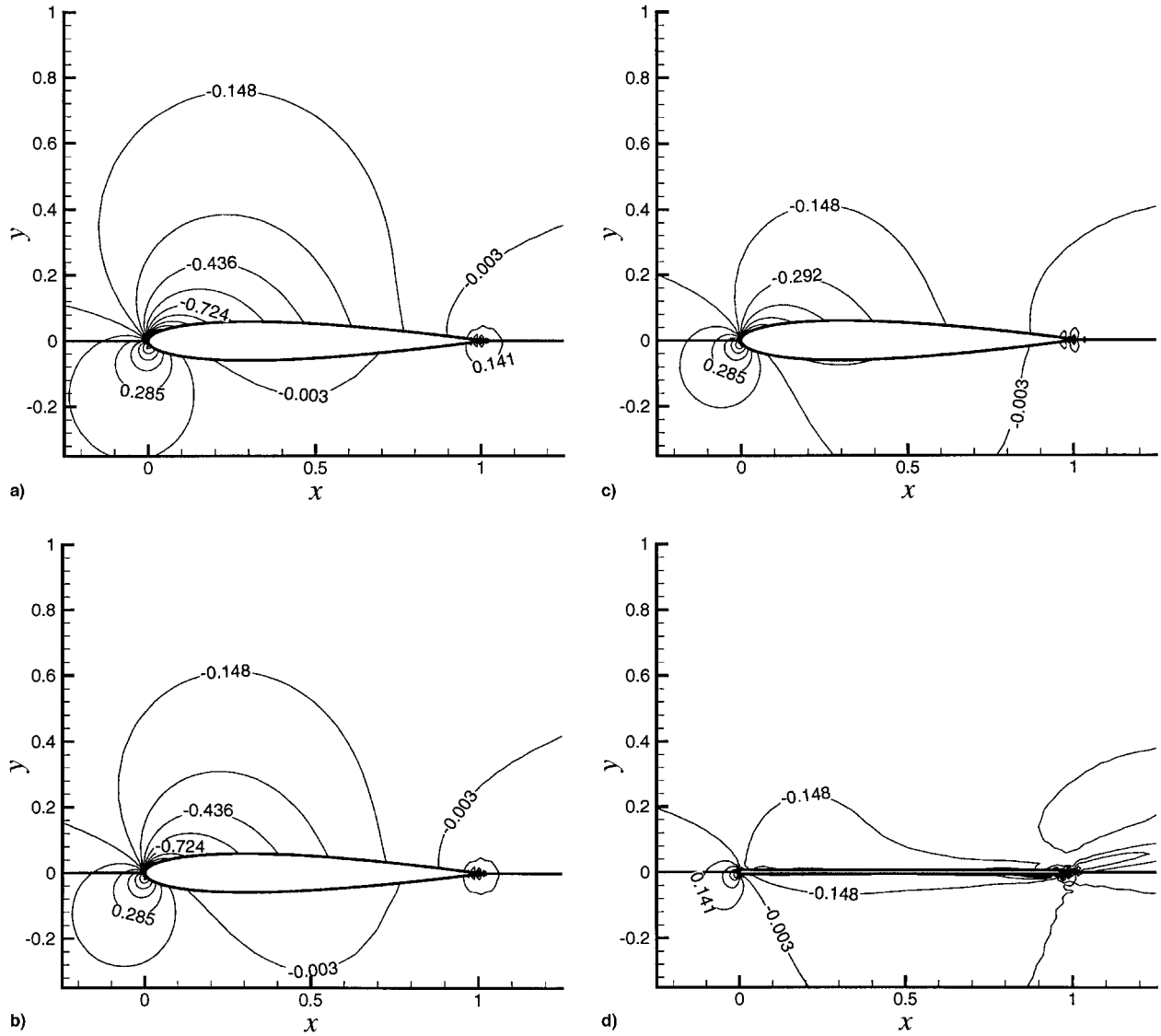

Fig. 7 Pressure coefficient contours for flow over a NACA 0012 wing. $M = 0.117$, $\alpha = 5$ deg, $b = 8.54$: a) root plane, $z = -4.27$; b) $z = -1.0$; c) $z = -0.1$; and d) tip plane, $z = 0.1$.

The experiments were conducted in a low-speed tunnel with a freestream velocity of 40 m/s and a Reynolds number around 5.3×10^5. The wing in the experiment had an aspect ratio of 8.66. Although Devenport et al.'s data extend to $x = 30$, which is beyond the present computational domain, comparisons can still be made up to $x = 10$. The simulations are performed on the IBM SP2 with RS6000 model 590 nodes with a high-speed switch. Sixteen processors are used for the calculations. The grid consists of two blocks of $177 \times 65 \times 85$. A total of 1.955 million points are used. To accelerate the convergence to steady state, a three-mesh-level multigrid sawtooth cycle is used. Figure 4 shows the convergence history of the density residual as a function of CPU minutes and cycles. The residual drops three orders of magnitude very quickly but then levels off. Comparisons of the solutions after 1200 cycles show very little difference from that after 2500 cycles. As far as the mean aerodynamics are concerned, the solution can be considered converged. However, to start an unsteady simulation using this mean flow, it is convenient to obtain convergence to machine zero. There are two contributing factors that stall the convergence. The first is the special operators that must be applied on the wing surface in the vicinity of the block boundary. Because these operators must be set explicitly, the switch in the artificial dissipation cannot be used to determine the scaling coefficients and stencil size for the smoothers. Hence, it is unlikely that the artificial dissipation will vary smoothly from the leading edge to other points around the airfoil. This problem is particularly acute at the corner of the tip. The same argument holds for the biased and reduced-order derivative operators used around the block interface at the leading edge and tip. However, complete convergence has been obtained in two dimensions using a similar approach. The three-dimensional nature of the current problem and the difficulties with the tip region do result in some additional difficulty in obtaining complete convergence. An additional problem, which actually results in higher levels of the residual, is at the boundary in the x–y plane off the tip. The tip vortex induces a swirling flow that attempts to move fluid in and out of this boundary. The Riemann conditions do not model this type of flow properly. Although this causes errors near the boundary, they are small compared with the variations in the mean flow caused by the presence of the wing.

The scalability of the multigrid code is investigated in Fig. 5. The CPU per grid point per cycle is used as a measure of performance for 8–64 processors. The problem requires too much memory to run on four nodes when each node has 128 Mbytes of memory. The figure shows that the code does scale relatively well up to 64 processors. All of the calculations are performed in a few hours on 16 nodes at a Mflop/s rate per node of 33. The total Mflop/s rate is 534. With 64 nodes, the code obtains nearly 2 Gflop/s. There is some degradation in performance as the number of processors is increased. This effect is exacerbated by the multigrid because much of the work is performed on smaller grids. The coarsest mesh is reduced by a factor of 64 compared to the finest mesh. Dividing this mesh among 64 processors results in only 326 points on each node. This produces a higher percentage of time spent sending messages, as shown in Fig. 6. The figure also accentuates the importance of fast communication for three-dimensional problems when entire planes of data must be sent to adjacent nodes. Still, the speed-up is fairly good.

Pressure coefficient contours at several positions along the span are presented in Fig. 7. The flow is two dimensional at the root plane where the symmetry condition is applied. A comparison of Figs. 7a and 7b shows that only a small variation in the distribution is obtained between the root and one chord length from the tip. Figures 7c and 7d show the distribution near the tip. The flow is considerably different in the rounded region of the tip shown in Fig. 7d. Almost no lift is generated in this region. A numerical integration of the pressure on the wing produces a dimensionless lift for the half-span of $F_L = 0.0132$. This can be compared with the results of classical lifting-line wing theory that can be found in any good text on aerodynamics such as Anderson.[21] The formula for the lift-curve slope is

$$\frac{dC_L}{d\alpha} = \frac{a_0}{1 + a_0(1 + \tau)/(\pi \mathrm{AR})} \tag{14}$$

$a_0 = 6.303$/rad is the lift-curve slope for the NACA 0012 airfoil section, and $\tau = 0.08$ accounts for the rectangular shape of the wing. The lift coefficient for the wing is then

$$C_L = \frac{dC_L}{d\alpha}\,\alpha \tag{15}$$

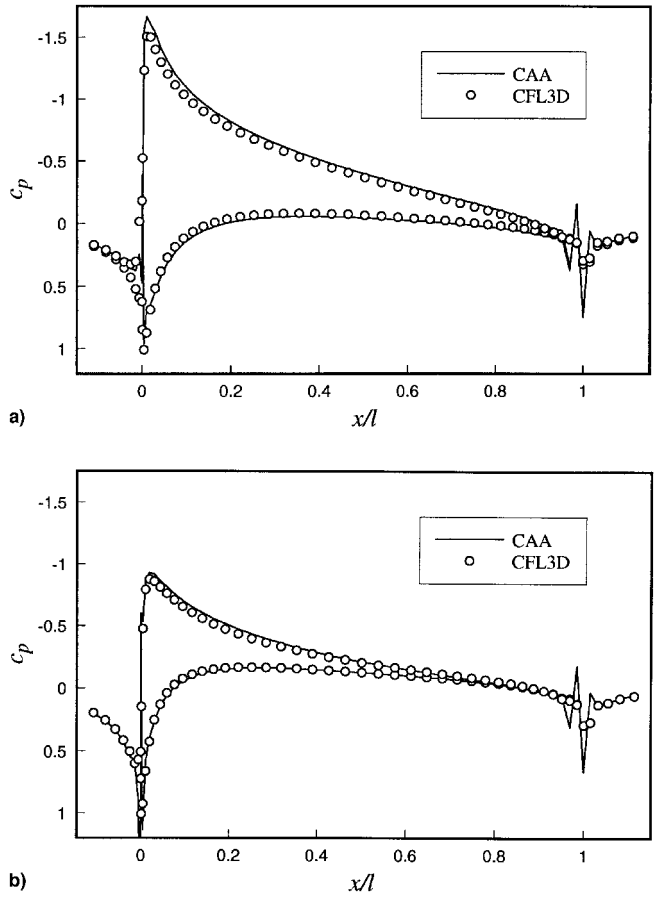

Fig. 8 Surface pressure coefficient distributions for flow over a NACA 0012 wing. $M = 0.117$, $\alpha = 5$ deg, $b = 8.54$: a) root plane, $z = -4.27$ and b) $z = -0.1$.

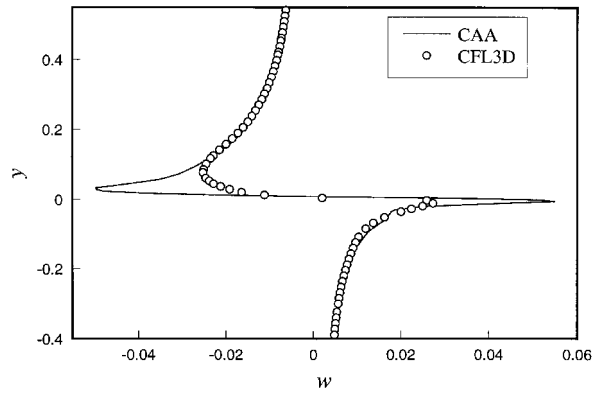

Fig. 9 Tangential velocity profiles through the vortex core at the trailing edge of a NACA 0012 wing. $M = 0.117$, $\alpha = 5$ deg, $b = 8.54$.

because the NACA 0012 is symmetric and has no lift at α = 0 deg. The resulting lift force is estimated to be $F_L = 0.0128$, which compares well with the numerical result. The pressure coefficient on the wing surface has also been compared with the results from CFL3D,[22] a well-established CFD code. It was run in an inviscid mode with the identical fine grid used with the CAA code. Figure 8 compares the solutions from the two methods. Because CFL3D is a low-order, implicit code, it is able to handle discontinuities much better than the CAA code. This is evidenced in the region near the trailing edge where the CFL3D solution remains smooth, whereas oscillations are evident in the CAA code's solution. However, the high-order, low-dissipation nature of the CAA scheme produces a much stronger tip vortex and enables it to resolve most of the flow features on a coarser mesh than typical CFD codes. Hence, the slight differences between the solutions in the c_p plots are not unexpected. The differences in the dissipation of the two methods is illustrated in Fig. 9, which compares the tangential velocity profiles through the tip vortex in the plane $x = 1$ that passes through the trailing edge of the wing. From the inception of the vortex the velocity change through the core is quite different from the two simulations, and the difference becomes greater as the vortex moves downstream.

To visualize the tip vortex, velocity vectors in several x–z planes are shown in Fig. 10. Four different stations in the streamwise direction are shown ranging from $x = 1.5$ to 10 (Figs. 10a–10d). In these figures the mean component of velocity in the y direction has been subtracted from the total v velocity to the make the vortex easier to identify. The vectors at the trailing edge are not shown because the presence of the body distorts the vortex and one mainly sees the flow going from under the wing to above it. After a half-chord, a vortex may be seen clearly in Fig. 10a. The sequence shows that the vortex center is displaced inboard and upward as it moves downstream. The vertical distance is somewhat exaggerated because the vortex is also convected upward by the mean flow. However, there is additional motion in this direction beyond that caused by the mean flow. The sequence also shows that the vortex increases in size and becomes somewhat weaker away from the wing. Because this is an inviscid simulation,

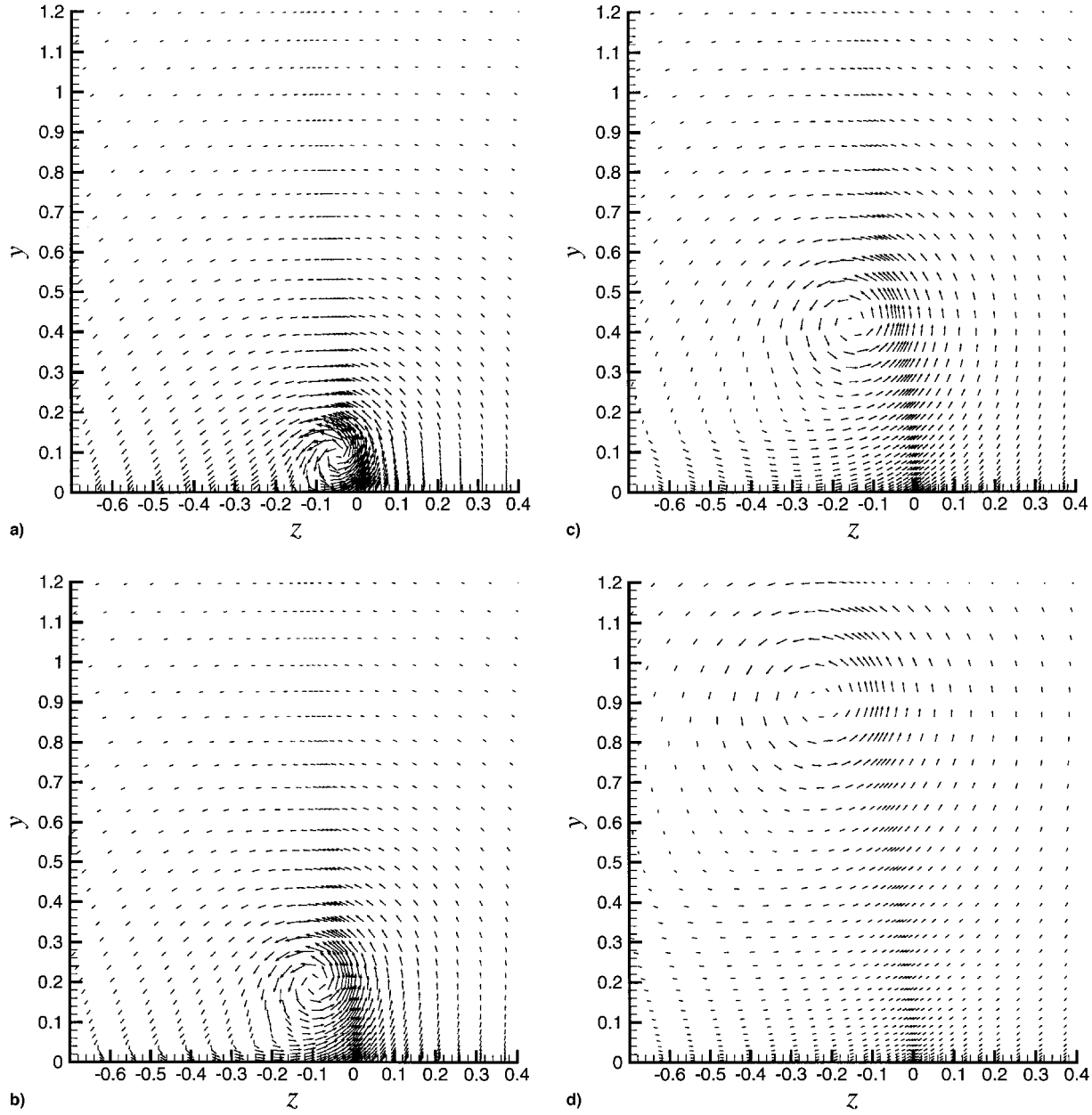

Fig. 10 Velocity vectors for flow over a NACA 0012 wing. $M = 0.117$, $\alpha = 5$ deg, $b = 8.54$. The mean vertical velocity has been removed. x = a) 1.5, b) 2.5, c) 5, and d) 10.

little or no decay should be obtained. However, numerical dissipation will cause a viscous-like decay if there is not sufficient resolution of the vortex. The solution in Fig. 10d represents the edge of the computational domain. The vortex is still clearly identifiable, indicating that the characteristic boundary conditions are able to allow the vortex to pass through with only minimal errors.

The pressure coefficient in the vortex at $x = 5$ is shown in Fig. 11. A fairly significant pressure drop clearly identifies the vortex. This pressure drop persists to the outflow boundary. The Mach number contours in the streamwise direction for this plane are shown in Fig. 12. The dark region represents a small wake. Because the problem is inviscid, there should be a vortex sheet behind the wing, but not a viscous wake associated with a boundary layer on the wing. However, the artificial dissipation produces a slight velocity deficit of about 10% near the wing surface. This deficit does not affect the other flow variables. At $x = 5$, Devenport et al.[10] found that the minimum value for the Mach number in the streamwise direction at the core of the vortex should be around 0.1. The numerical data show higher velocities. This should be expected because the no-slip condition is not applied. The real vortex core is formed around the tip of the wing where all of the velocities are zero. This part of the physics, that is missed by the inviscid model, produces vortices that are different from those measured in experiments.

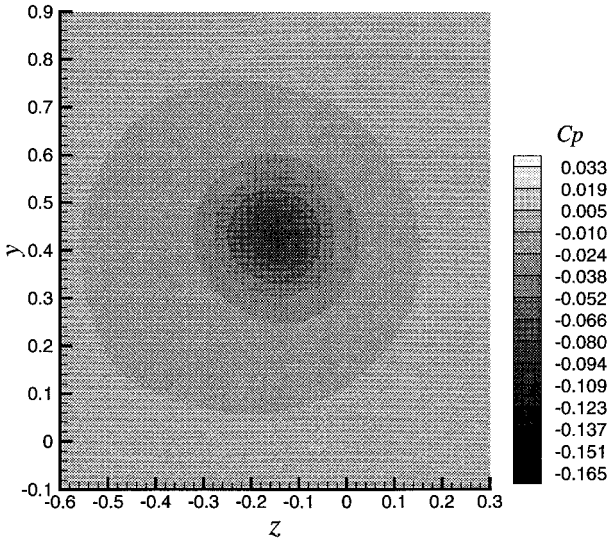

Fig. 11 Pressure coefficients contours for flow over a NACA 0012 wing in the $x = 2$ plane. $M = 0.117$, $\alpha = 5$ deg, $b = 8.54$.

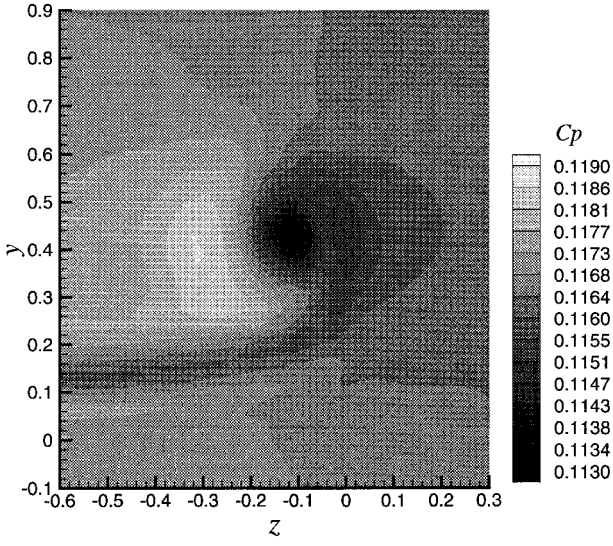

Fig. 12 Mach number contours for flow over a NACA 0012 wing in the $x = 2$ plane. $M = 0.117$, $\alpha = 5$ deg, $b = 8.54$.

To examine the dynamics of the vortex as it propagates away from the wing, data are extracted through the vortex core at different x locations. The core is identified by examining vector plots of the velocities similar to those shown in Fig. 10. A postprocessing program is used to extract data along the y and z directions through the core. The variation of the vertical velocity with z is shown in Fig. 13. The mean contribution to the vertical velocity is 0.01, which accounts for the offset in the curves. Comparisons are made between solutions from the original grid and one reduced by a factor of 2 in each direction. In addition the coarse mesh only extends to $x = 4.5$ in the downstream direction. The solution on the coarse $61 \times 33 \times 43$ grid in Fig. 13a exhibits a rapid diffusion of the vortex. Furthermore, the peak velocities are small compared with those from the fine grid shown in Fig. 13b. On this coarse mesh, the tip is resolved poorly and resembles a wedge. The solution on the finer grid shows only minimal diffusion of the vortex. It is interesting that most of the decay in the velocity difference is associated with the positive peak. The negative peak decays slowly with downstream distance. It appears that most of the decay is associated with the vortex eliminating its asymmetry that is caused by the interference with the wing. While near the wing the maximum velocity is associated with the flow moving up around the tip. The negative velocity is inhibited by the no-penetration condition at the wall, so that its magnitude never becomes as large. As the vortex moves downstream, the positive peak decreases to obtain nearly the same magnitude of velocity as the negative peak. This is similar for the tangential velocity w shown in Fig. 14. Figure 14a again shows that the solution is relatively poor on the coarse grid. There is not enough resolution to generate the correct

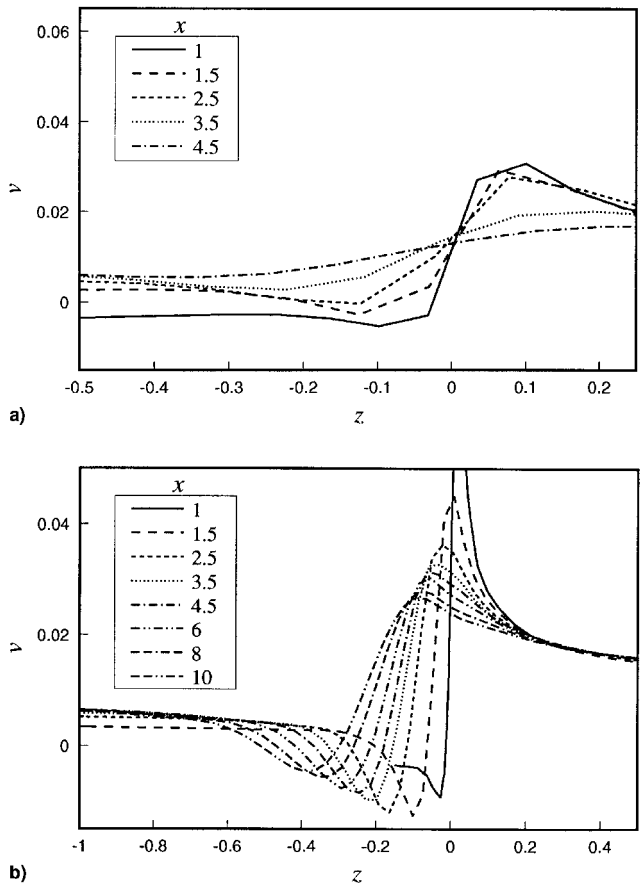

Fig. 13 Vertical velocity profiles through the vortex core for a NACA 0012 wing. $M = 0.117$, $\alpha = 5$ deg, $b = 8.54$: a) $61 \times 33 \times 43$ and b) $177 \times 65 \times 85$.

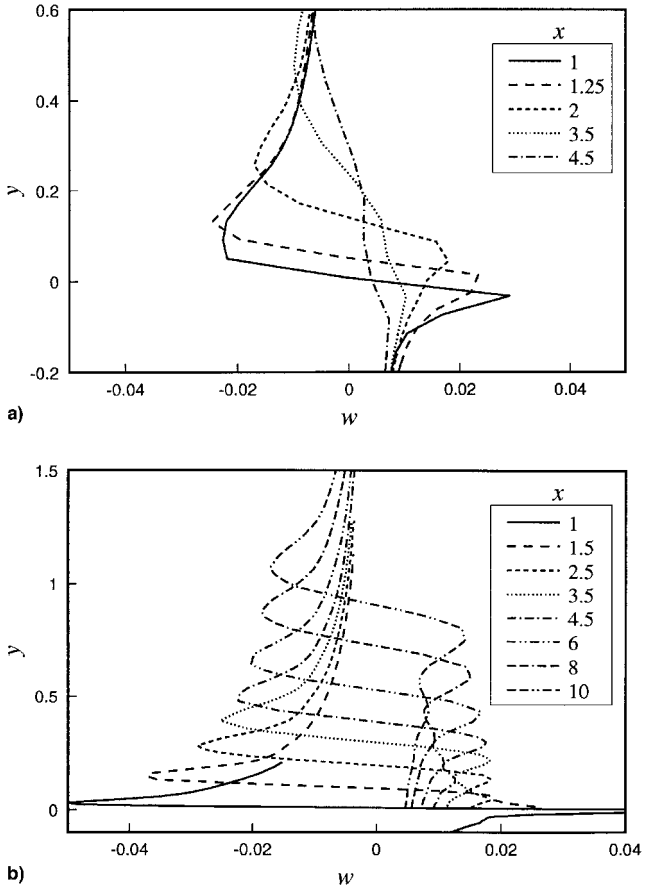

Fig. 14 Tangential velocity profiles through the vortex core for a NACA 0012 wing. M = 0.117, α = 5 deg, b = 8.54: a) 61 × 33 × 43 and b) 177 × 65 × 85.

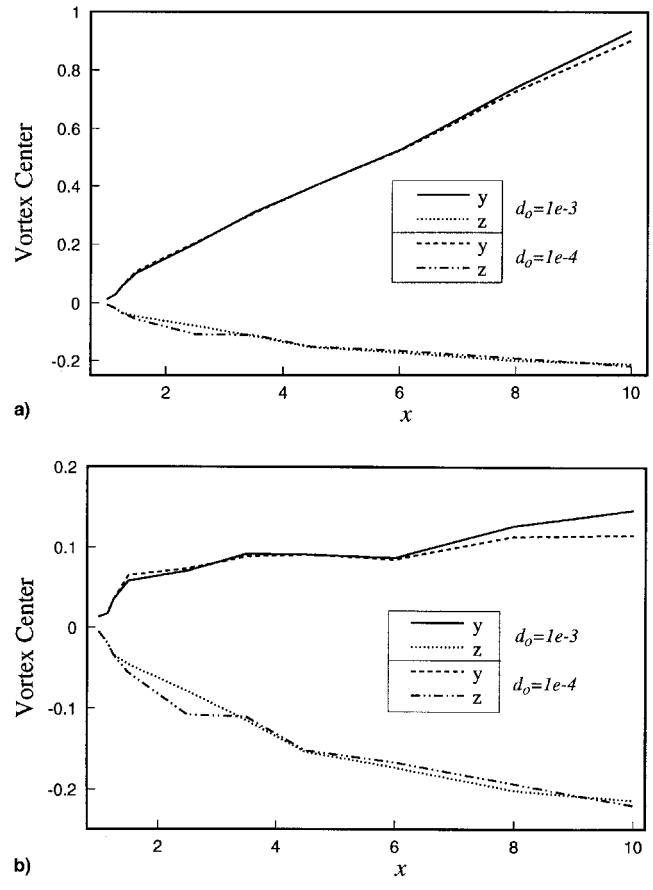

Fig. 15 Location of the tip vortex core as a function of downstream distance for flow over a NACA 0012 wing. M = 0.117, α = 5 deg, b = 8.54. y measured from a) airfoil axis and b) freestream vector.

strength or maintain the vortex. Figure 14 shows that the positive peak in the w velocity changes slowly, whereas the negative peak decreases to almost the same magnitude as the positive peak. Again, it is surmised that this is an adjustment by the vortex to remove its initial asymmetry. Nonetheless, the effects of the no-slip condition and viscosity have been neglected and they could alter this development. The additional decay is probably a result of the artificial dissipation and grid resolution. Because the scheme has relatively little background dissipation, a finer grid would be required to improve the results. Calculations with smaller values of the dissipation have been included to demonstrate that they have only a small effect on the solution and are described next. However, the alternative choice of increasing the grid resolution everywhere is impractical.

The position of the vortex core as a function of downstream distance is shown in Fig. 15. Recall that the $y = 0$, $z = 0$ position refers to the vertical center of the wing tip. Two different values of the dissipation are used. The larger value of $d_0 = 1e - 3$ is the baseline. The lower value of $d_0 = 1e - 4$ is actually too small to be used in an unsteady calculation and is barely enough to suppress odd–even decoupling. Figure 15 shows that the background dissipation has very little effect on the position of the vortex. The solutions have the correct displacement of the vortex upward and in toward the root. This motion is caused by the induced velocities of the tip vortices and the vortex sheet behind the wing. In Fig. 15a, the location of the vortex core in the y direction is measured from the airfoil axis. In Fig. 15b it is measured from the freestream vector. This shows that the motion in the y and z directions is similar when the convection by the mean flow is excluded. The position of the vortex is subject to wandering in experiments that makes it extremely difficult to identify the position of the vortex core. Devenport et al.[10] made careful measurements to identify the wandering and correct the data accordingly. At $x = 5$ the spanwise displacement was found to be $z = -0.17$. This is close to the value found in the numerical simulation. At $x = 10$ Devenport et al. measured the displacement to be around $z = -0.35$, which is much larger than that from the simulation. In the experiment the vertical displacement was measured from the lowest point in the wake centerline. This should be close to the distance from the freestream vector. The vertical displacement was 0.18 at $x = 5$ and 0.28 at $x = 10$. The measured vertical displacement is considerably larger than that obtained from the simulation, but the difference in the reference location may be partially responsible for the discrepancy. The displacements typically have a square-root variation with downstream position. Devenport et al.'s data show this very clearly between $x = 5$ and 30.

The vortex core size and the velocity difference across the core are shown in Fig. 16. The core size is taken to be the distance between the peaks in the velocity profiles shown in Figs. 13 and 14. The core size in Fig. 16a shows a rapid increase just past the the trailing edge. After this initial period, the core size increases slowly with downstream distance. However, the core size is consistently larger for the higher background dissipation. For each case the core size measured in the y and z directions are also similar, and the velocity change across the vortex shown in Fig. 16b also becomes nearly identical after $x = 2.5$. Devenport et al.'s experiment at $x = 5$ showed the core size to be approximately 0.074, which is less than half that obtained in the simulation. Furthermore, the velocity difference from the experiment is around 0.067, which is slightly above that found in the simulation. However, Devenport et al.'s data show little change in the vortex parameters

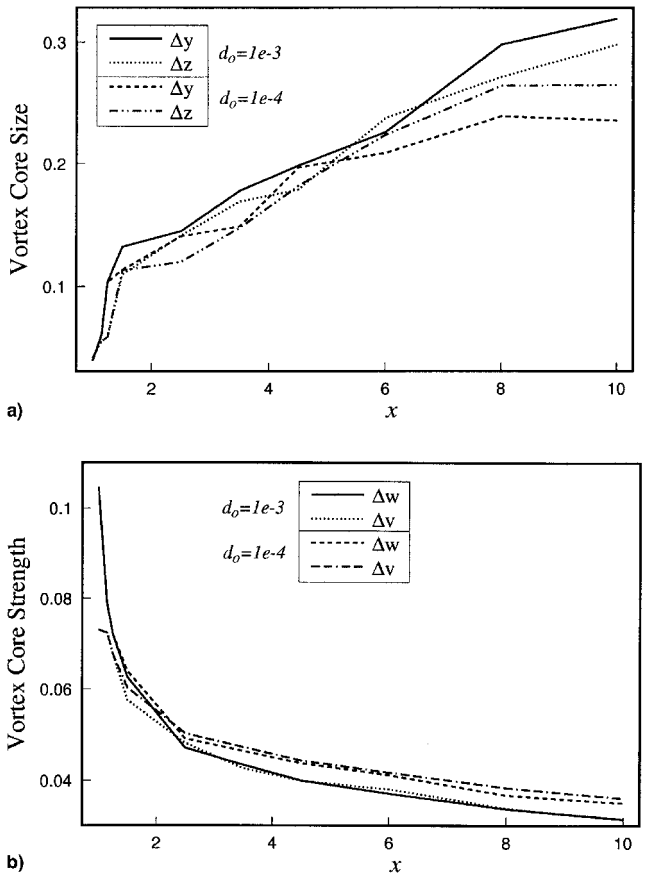

Fig. 16 Tip vortex core size and maximum velocity change for flow over a NACA 0012 wing. M = 0.117, α = 5 deg, b = 8.54: a) vortex core size and b) velocity change across the vortex core.

between x = 5 and 30. One would expect that the vortex in the simulation would continue to exhibit some decay if the computational domain were extended.

The circulation for the tip vortex is calculated by integrating numerically the velocity field around a closed contour of varying radius. The circulation is given by

$$\Gamma = \oint \boldsymbol{V} \cdot \mathrm{d}\boldsymbol{s} \tag{16}$$

Figure 17 shows the circulation as a function of the radial size of the contour at several downstream locations. The circulation is relatively insensitive to the downstream position. Hence, the simulated vortex appears to conserve circulation. The circulation at x = 10 is slightly different from that at other locations for small radii. This is indicative of the spreading of the vortex. The circulation is normalized by the theoretical circulation at the root given by

$$\Gamma_0 = (2/\pi) M_\infty C_L \tag{17}$$

determined by assuming an elliptical load distribution. The wing lift coefficient is 0.439. This yields Γ_0 = 0.0327. The plot also reveals that much of the vorticity is outside of the vortex core. According to the lifting-line theory, this is the part of the vortex sheet that is generated by the wing. Far downstream, the vortex sheet will roll up completely into the tip vortices. At this early stage of development, much of the vortex sheet is still intact. Devenport et al.[10] calculated the circulation from their experiment. Some of these data are included in Fig. 17. On a semilog plot it varies nearly linearly outside of the core. This is in good agreement with the simulation and is also found using lifting-line theory. From the experiments Γ/Γ_0 = 0.41 at r = 0.1, and Γ/Γ_0 = 0.76 at r = 0.6. These values are very close to those determined from the simulation.

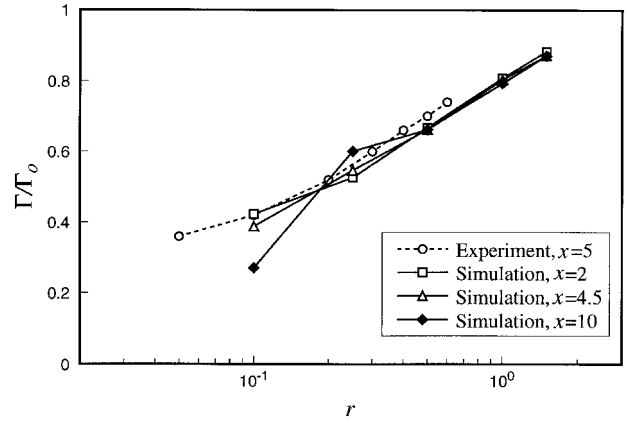

Fig. 17 Circulation in the tip vortex as a function of radius for flow over a NACA 0012 wing. M = 0.117, α = 5 deg, b = 8.54. Experimental data are from Devenport et al.[10]

Conclusions

The steady simulation of a relatively complex aircraft component using the high-accuracy operators of CAA algorithms moves numerical studies of acoustics closer to the goal of providing designers with useful information about realistic configurations. However, considerable work remains to be done. Although the current simulation preserves the tip vortex relatively well compared to modern CFD schemes, the decay is still too large. Even if the hypothesis about the vortex adjustment to eliminate its initial asymmetry is correct, the decay beyond this point is larger than that observed in the experiment. The core size of the vortex in the simulation is at least double the size observed in the experiment after only a few chords of propagation. Furthermore, the initial development of the vortex is likely to be altered significantly by viscosity. Because the vortex remains extremely tight, a very fine grid would be required to resolve the gradients through the vortex core. However, a time-accurate simulation on a viscous grid would be prohibitive because of the time-step restriction. Furthermore, the generation of a structured grid in three dimensions is a difficult and time-consuming process. The H–H mesh used in this study is far from ideal because of the discontinuity in the grid metrics near the edges of the wing. The special treatment used in this research allows solutions to be obtained, but oscillations are still evident in these regions. These oscillations not only inhibit convergence, but they also generate errors, primarily in the form of entropy.

These are still significant issues that must be addressed to obtain the maximum accuracy from CAA calculations. However, some useful information could be obtained from time-dependent simulations using the present method. It may not be feasible to address all of the problems immediately, but this should not deter researchers from using CAA schemes for problems where they are readily applicable.

References

[1]Lockard, D. P., and Morris, P. J., "The Radiated Noise from Airfoils in Realistic Mean Flows," AIAA Paper 97-0286, Jan. 1997.

[2]George, A. R., Najjar, F. E., and Kim, Y. N., "Noise Due to Tip Vortex Formation on Lifting Rotors," AIAA Paper 80-1010, June 1980.

[3]Kramer, E., Hertel, J., and Wagner, S., "Computation of Subsonic and Transonic Helicopter Rotor Flow Using Euler Equations," *Vertica*, Vol. 12, No. 3, 1988, pp. 279–291.

[4]Srinivasan, G. R., Baeder, J. D., Obayashi, S., and McCroskey, W. J., "Flowfield of a Lifting Hovering Rotor—A Navier-Stokes Simu-

lation," 16th European Rotorcraft Forum, Glasgow, Scotland, Sept. 1990.

[5]Strawn, R. C., "Wing Tip Vortex calculations with an Unstructured Adaptive-Grid Euler Solver," 47th Annual Forum of the American Helicopter Society, Phoenix, AZ, May 1991.

[6]Francis, M. S., and Kennedy, D. A., "Formation of a Trailing Vortex," *Journal of Aircraft*, Vol. 16, No. 3, 1979, pp. 148–154.

[7]Felker, F. F., Piziali, R. A., and Gall, J., "Spanwise Loading Distribution and Wake Velocity Surveys of a Semi-Span Wing," NASA-TM-84213, Feb. 1982.

[8]McAlister, K. W., and Takahashi, R. K., "NACA0012 Wing Pressure and Trailing Vortex Measurements," NASA-TP-3151, Nov. 1991.

[9]Shekarriz, A., Fu, T. C., and Katz, J., "Near-Field Behavior of a Tip Vortex," *AIAA Journal*, Vol. 31, No. 1, 1993, pp. 112–118.

[10]Devenport, W. J., Rife, M. C., Liapis, S. I., and Follin, G. J., "The Structure and Development of a Wing-Tip Vortex," *Journal of Fluid Mechanics*, Vol. 312, March 1996, pp. 67–106.

[11]Lockard, D. P., and Morris, P. J., "A Parallel Implementation of a Computational Aeroacoustic Algorithm for Airfoil Noise," AIAA Paper 96-1754, May 1996.

[12]Lockard, D. P., "Simulations of the Loading and Radiated Sound of Airfoils and Wings in Unsteady Flow Using Computational Aeroacoustics and Parallel Computers," Ph.D. Dissertation, Dept. of Aerospace Engineering, Pennsylvania State Univ., University Park, PA, Aug. 1997.

[13]Tam, C. K. W., and Webb, J. C., "Dispersion-Relation-Preserving Finite Difference Schemes for Computational Aeroacoustics," *Journal of Computational Physics*, Vol. 107, No. 2, 1993, pp. 262–281.

[14]Lockard, D. P., Brentner, K. S., and Atkins, H. L., "High-Accuracy Algorithms for Computational Aeroacoustics," *AIAA Journal*, Vol. 33, No. 2, 1995, pp. 246–251.

[15]Hirsch, C., *Numerical Computation of Internal and External Flows*, Vol. 2, Wiley, New York, 1990, pp. 334–337, Chap. 10.

[16]Thompson, K. W., "Time-Dependent Boundary Conditions for Hyperbolic Systems, II," *Journal of Computational Physics*, Vol. 89, No. 2, 1989, pp. 439–461.

[17]Jameson, A., Schmidt, W., and Turkel, E., "Numerical Solution of the Euler Equations by Finite-Volume Methods Using Runge-Kutta Time-Stepping Schemes," AIAA Paper 81-1259, June 1981.

[18]Tam, C. K. W., and Dong, Z., "Radiation and Outflow Boundary Conditions for Direct Computation of Acoustic and Flow Disturbances in a Nonuniform Mean Flow," CEAS/AIAA Paper 95-007, June 1995.

[19]Jameson, A., "Multigrid Algorithms for Compressible Flow Calculations," *Multigrid Methods II, Proceedings of the 2nd European Conference on Multigrid Methods*, No. 1228 in Lecture Notes in Mathematics, Springer–Verlag, London, 1986, pp. 166–201.

[20]Briggs, W. L., *A Multigrid Tutorial*, Society for Industrial and Applied Mathematics, SIAM, Philadelphia, PA, 1987.

[21]Anderson, J. D., *Fundamentals of Aerodynamics*, 2nd ed., McGraw–Hill, New York, 1991, pp. 237–258, Chap. 5.

[22]Thomas, J. L., Krist, S., and Anderson, W., "Navier-Stokes Computations of Vortical Flows over Low-Aspect-Ratio Wings," *AIAA Journal*, Vol. 28, No. 2, 1990, pp. 205–212.